

Communication

Potassium Acetate-Based Treatment for Thermally Co-Evaporated Perovskite Solar Cells

Jia Li ¹, Hao Wang ¹, Herlina Arianita Dewi ¹, Nripan Mathews ^{1,2,*}, Subodh Mhaisalkar ^{1,2,*} and Annalisa Bruno ^{1,*}

¹ Energy Research Institute @ NTU (ERI@N), Nanyang Technological University, Singapore 637553, Singapore; li-jia@ntu.edu.sg (J.L.); wanghao@ntu.edu.sg (H.W.); herlina@ntu.edu.sg (H.A.D.)

² School of Materials Science & Engineering, Nanyang Technological University, Singapore 639798, Singapore

* Correspondence: nripan@ntu.edu.sg (N.M.); subodh@ntu.edu.sg (S.M.); annalisa@ntu.edu.sg (A.B.)

Received: 28 October 2020; Accepted: 23 November 2020; Published: 28 November 2020



Abstract: Thermal evaporation is a very successful and widely adopted coating technique for the deposition of organic and inorganic materials on rough and textured surfaces and over large areas. Indeed, this technique is extensively used in the semiconductor industry for the fabrication of organic light emitting diodes (OLEDs) and is commonly used in displays. In the last few years, thermal evaporated perovskite solar cells (PSCs) have also shown the potential to reach high power conversion efficiency (PCE) both on small and over large area devices. In this work, we present a detailed optimization of the potassium-based surface treatment used to improve the performances of our MAPbI₃ PSCs fabricated using the thermal co-evaporation technique. Small area planar n-i-p PSCs with an active area of 0.16 cm² achieved PCEs above 19% and the large area PSCs with an active area of 1 cm² reached 18.1%. These un-encapsulated PSCs also proved an excellent long-term shelf stability maintaining 90% of their initial PCEs for over six months when stored at ambient temperature.

Keywords: co-evaporated; MAPbI₃; metal halide perovskite; perovskite solar cells; potassium treatment

1. Introduction

Metal-halide perovskite materials brought a recent revolution in the photovoltaic [1,2] and optoelectronics fields [3]. Their excellent performances are mainly related to their intrinsic outstanding optoelectronic properties [4–8]. In addition, the metal-halide perovskite fabrication versatility [9–11] is a key feature that makes the perovskite-based optoelectronic technologies promising for their future industrialization manufacturing in a large wide range of applications.

On the other hand, vacuum deposition techniques are widely used in the semiconductor industry, as they can guarantee good uniformity over a large area, provide conformal coverage on even rough substrate surface, and enable precise control of the layer thickness. Indeed, also the state-of-the-art organic light emitting diodes (OLEDs) and displays are fabricated through thermal evaporation deposition processes. Consequently, the co-evaporation process [12–14] represents the most viable option for the integration of perovskite-based optoelectronic devices, like solar cells, OLED, other light-emitting devices, photodetectors, and transistors, with the existing industrial lines.

Perovskite solar cells (PSCs) have achieved a record power conversion efficiency (PCE) of 25.5% [15] in slightly more than a decade [16], and their operational stability is now also rapidly improving [17–19]. Currently, the best-performing PSCs are still yielded by the favored lab-scale solution-processed techniques such as the spin-coating method on small scale (~0.1 cm²) devices [20–24]. These solution processes involve the use of a large number of hazardous solvents and have constraints in large scale fabrication due to relatively poor uniformity over a large area. Few groups have also

explored the solvent-free route [25] or solution-vacuum hybrid methods, such as hybrid chemical vapor deposition and cation exchange method [26,27]. The good uniformity over large substrates together with the possibility of providing excellent conformal coverage on even rough substrate surface represent the thermal co-evaporation highly attractive features that are indeed critical characteristics for developing high performing perovskite solar modules and tandem solar cells [28–30].

Our group has recently demonstrated PSCs by vacuum co-evaporation with a champion PCE of 20.28% over small area and the first co-evaporated perovskite solar modules with a PCE of 18.1% over an active area of 21 cm² employing SnO₂ as the electron transport layer. [12] To improve the PSCs performance, we implemented a surface treatment strategy based on methyl ammonium iodide (MAI) and potassium acetate (KAc) to improve the charge transport at the grain boundaries [31]. In this work, we present the detailed study and of the effect of MAI treatment and KAc treatment and a combination of MAI + KAc treatment on the PSCs performances. The step-by-step optimization process has led us to demonstrate a PSCs based on TiO₂ as electron transport layer, with PCEs of 19.0% with an active area of 0.16 cm² and 18.1% for 1 cm² active area without employing any antireflection coating. These un-encapsulated TiO₂ PSCs also showed an extremely promising long-term stability when stored in dark and under continuous operation in humidity environments.

2. Experimental Section

2.1. Device Fabrication

The full device structure is presented in Figure 1a. The step-by-step-cleaning and preparation procedure is presented here after. Fluorine doped Tin Oxide (FTO) glass substrates (with a resistivity of 15 ohm/square) were ultra-sonicated in soap (brand: Decon 90, Hove, UK), deionized water, and subsequently ethyl alcohol for 15 min, respectively, and then dried in nitrogen flow. They were consequently UV–ozone treated (Novascan PSD Pro Series, Boone, IA, USA) for 20 min at room temperature.

2.1.1. Titanium Oxide (TiO₂)

The solution for the TiO₂ was prepared by mixing 11 g tetrabutyltitnate, 45 g anhydrous ethanol, 3.5 g diethanolamine, and 1.5 g deionized water. TiO₂ layer was spin coated by using a 1 step program (5000 r.p.m. for 20 s) on as preheated (at 80 °C for 10 min) substrate. The film was then heated to 500 °C for 60 min to form the planar TiO₂ layers. The Phenyl-C61-butyric acid methyl ester (PCBM) solution was prepared by dissolving 3 mg of PCBM (Sigma-Aldrich, St. Louis, MO, USA) in 1 mL of Chlorobenzene (CBZ) (Sigma-Aldrich, St. Louis, MO, USA). The substrates were then treated with UV–ozone for 20 min at 100 °C. The PCBM layer was deposited by spin coating in a single step process at 3000 r.p.m. for 30 s. Then the substrates are transferred into the evaporation chamber and the vacuum was pumped down to 10^{−6} Torr before evaporating MAPbI₃.

2.1.2. Perovskite

The perovskite layer was formed by co-evaporating PbI₂ (TCI, Tokyo, Japan) and MAI (Lumtec, Taiwan) powders. The temperature of PbI₂ and MAI were kept constants at 260 °C and 100 °C, respectively. The MAPbI₃ perovskite film was post-treated by three different methods (Table 1): (i) pure MAI solution in isopropyl alcohol (IPA), with concentrations varying from 12.5 to 62.5 mM, (ii) with 20 mM KAc solution, or (iii) KAc and MAI (1:1 in molar ratio) mixed solution in IPA, with concentrations varying from 10 to 40 mM. For the three passivation strategies, a dynamic spin-coating deposition method has been used, with a speed 3000 r.p.m. for 30 s. The as-prepared film and post-treated film were annealed at 100 °C for 30 min.

2.1.3. 2,2',7,7'-Tetrakis[N,N-di(4-methoxyphenyl)amino]-9,9'-spirobifluorene (Spiro-OMeTAD)

The Spiro-OMeTAD solution is prepared by dissolving 72.3 mg of Spiro-OMeTAD powder (Lumtec, Taiwan) in 1 mL of chlorobenzene. A total of 28.5 μL of 4-tert-Butylpyridine (TBP) solution and 17.5 μL

bis(trifluoromethane)sulfonamide lithium (Li-TFSI) salt solution (520 mg/mL in acetonitrile (ACN)) were added, and the final solution was stirred for 10 min. Spiro-OMeTAD was spin-coated with a speed of 4000 r.p.m. on the MAPbI₃ thin film after the samples were cooled down to room temperature.

Table 1. Surface passivation methods for MAPbI₃ active layer.

Methods	Surface Passivation	Concentration (mM)
Method 1	MAI	0–62.5
Method 2	KAc	20
Method 3	MAI+KAc	0–40

2.1.4. Gold Electrode

As top electrode, a 100 nm thin film of gold was thermally evaporated on the samples using a shadow mask to define the area.

2.2. Device Characterization

The photovoltaic current density–voltage (J–V) curves were measured under simulated air mass 1.5 (AM 1.5) sunlight (Newport 94043A, Beijing, China) which is calibrated by a standard silicon solar cell. J–V was measured in air without thermal stabilization and with a relative humidity (RH) of 70%. The incident photon-to-current conversion efficiency (IPCE) was measured by using a PVE300 (Bentham, London, UK), with a dual xenon/quartz halogen light source in DC mode Newport Oriel Sol3ATM solar simulator with a 450-watt Xenon lamp.

2.3. Morphology Film Characterization

The MAPbI₃ thin films were deposited on glass/FTO substrates and the morphology was characterized using Field Emission Scanning Electron Microscope (FESEM) from JEOL (JSM-7600F, JEOL USA Inc., Essex County, MA, USA).

3. Results

The planar n-i-p architecture of the PSC structure implemented in this work is reported in Figure 1a and the fabrication process described in the experimental section. The n-i-p architecture is still the device structure able to deliver the highest PCEs for PSCs.

In this work, the MAPbI₃ absorbing layer has been deposited by thermally co-evaporating MAI and PbI₂, as schematically represented in Figure 1b, in a double source chamber keeping the evaporation temperatures at 100 °C and 260 °C following the optimized procedures described in our previous work [12]. Details of the deposition procedure are also systematically reported in the experimental section. The device architecture includes a TiO₂ layer as electron transport layer (ETL), deposited on top of FTO glass. A thin PCBM layer has been used on top of the ETL to achieve a better carrier-selective interface with the co-evaporated MAPbI₃ absorber layer [12]. On top of perovskite, Spiro-OMeTAD is used as hole transport material (HTL) and a thin Au layer act as a top electrode. Using the as-deposited MAPbI₃, the PSCs achieved a PCE just slightly below 18%, as shown for the untreated devices (black dots) in Figure 1c. To improve the photovoltaic performances, we optimize here the step by step the methylammonium iodide/potassium acetate (MAI + KAc) treatment. The main goal of the treatment is to reduce the nonstoichiometric composition on the surface and within the bulk (PbI₂ excess) which would lead to the presence of under-coordinated species and minimizing the surface defects [31]. Indeed, the under-coordinated sites are detrimental to the PSC. Hereafter, we first analyze the effects of each component of the treatment separately on the photovoltaic performances of the PSCs and subsequently, and then we applied both the components together.

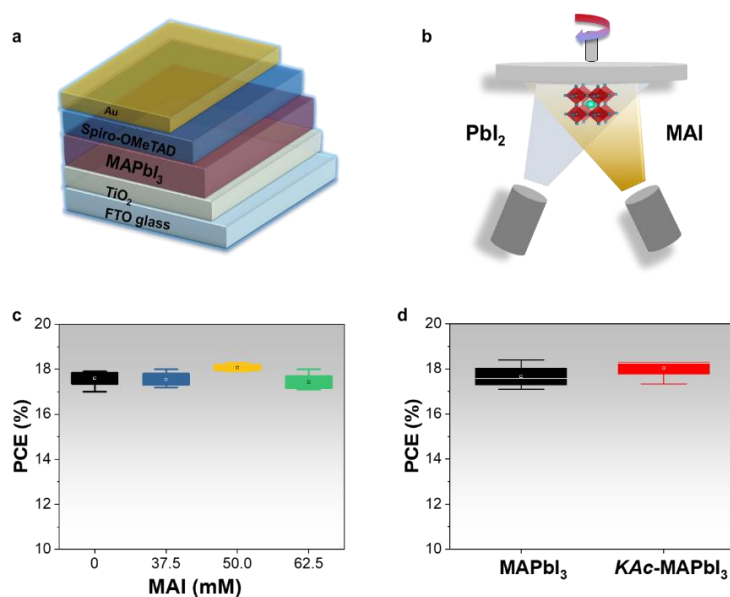


Figure 1. MAPbI₃ planar n-i-p device structure. (a) Schematic of perovskite solar cell device structure. (b) Schematic of the thermal co-evaporation of MAPbI₃ using methyl ammonium iodide (MAI) and lead iodide (PbI₂) precursors. (c) Power conversion efficiency (PCE) distributions as a function of the MAI concentration used for the spin coating treatment. (d) PCE distributions as a function of the potassium acetate (KAc) treatment.

The MAPbI₃ film was post-treated by three different approaches: (i) pure MAI solution, (ii) pure KAc solution, and (iii) KAc and MAI mixture in a 1:1 in molar ratio in IPA solution. The specific concentrations and experimental preparation conditions have been reported in the Experimental Section and summarized in Table 1. Indeed, since the XDR of the thin (~100 nm thick) MAPbI₃ films, reported in a previous paper [32], shows a small PbI₂ excess on the surface, our first step to improve the photovoltaic performances of the MAPbI₃ PSCs was based on a pure MAI surface treatment aiming to balance the stoichiometry. Figure 1c shows the photovoltaic parameter of an untreated MAPbI₃ PSCs together with the ones of PSCs where the active layers were treated with different MAI concentrations varying from 12.5 to 62.5 mM. The best working conditions were identified for a concentration of 50 mM. Figure S1 shows the trends for the photovoltaic parameters (V_{oc} , J_{sc} , and FF) of the treated and untreated PSCs, where it is clear that the most appreciable improvements are on both the V_{oc} and the J_{sc} . We can also observe that for treatment concentration of 50 mM, the spread was reduced. The data are also summarized in Table 2.

Table 2. Perovskite solar cells' (PSCs) photovoltaic parameters of the MAPbI₃ PSCs with MAI treatment. For each condition, the J_{sc} , V_{oc} , FF, and PCE average values were measured in backward scanning mode. PCEs for the champion PSCs are also reported.

MAI Treatment (mM)	V_{oc}^{av} (V)	J_{sc}^{av} (mA/cm ²)	FF ^{av} (%)	PCE ^{av} (%)	PCE ^{cham} (%)
0	1.101 ± 0.001	21.1 ± 0.1	75 ± 1	17.6 ± 0.3	17.9
37.5	1.093 ± 0.005	20.9 ± 0.3	76.6 ± 0.6	17.6 ± 0.4	18.0
50	1.108 ± 0.005	21.4 ± 0.2	76.3 ± 0.5	18.1 ± 0.2	18.3
62.5	1.103 ± 0.005	21.1 ± 0.5	73.9 ± 3.2	17.4 ± 0.6	18.0

The FESEM images of the as-deposited MAPbI₃ film and the MAPbI₃ film treated with 50 mM of MAI, show also different morphologies. The as-deposited MAPbI₃ has relatively small grain size in the range of 90 to 140 nm and some pinholes are visible, Figure S2a. When the MAI treatment is applied, the MAPbI₃ grains becomes bigger with average sizes of 130–250 nm, and the number of pinholes is reduced as compared to the pure MAPbI₃. However, the film shows relatively poor uniformity over large area (Figure S2b).

On the other hand, when the thin MAPbI₃ films are treated just with potassium acetate, no significant improvements on the PCEs were observed, Figure 1d. Indeed, the improvement on the V_{oc} is remarkable, Figure S3a. The potassium, K⁺, in the potassium acetate can passivate the defect in the surface and the at the grain boundary and so resulting in an improved V_{oc}, with a similar mechanism as the one described by Abdi-Jalebi et al. [31] and discussed in our previous work [12]. Although at the same time, the J_{sc} was instead significantly reduced. The data are also summarized in Table 3. At the same time, the FESEM images of the as-deposited MAPbI₃ film and the MAPbI₃ film treated with 20 mM of KAc, also show different morphologies. With the KAc treatment, the grain sizes of the MAPbI₃ are enlarged to 180–250 nm, and the large area coverage improves although few pinholes still visible in the film which could act as recombination points, Figure S2c.

Table 3. PSCs' photovoltaic parameters of the MAPbI₃ PSCs with KAc treatment. The J_{sc}, V_{oc}, FF, and PCE average values were measured in backward scanning mode. PCEs for the champion PSCs are also reported.

KAc Treatment (mM)	V _{oc} ^{av} (V)	J _{sc} ^{av} (mA/cm ²)	FF ^{av} (%)	PCE ^{av} (%)	PCE ^{cham} (%)
0	1.11 ± 0.02	21.4 ± 0.5	75 ± 2	17.7 ± 0.7	18.4
20	1.139 ± 0.005	20.8 ± 0.7	74.7 ± 0.3	18.0 ± 0.3	18.3

Differently, when both the MAI and KAc treatments are jointly applied on the MAPbI₃ thin films, the performances of PSCs significantly improved, Figure 2a. Indeed, we can observe that for all the concentrations of the MAI + KAc treatment used, both the V_{oc} and the FF improve (Figure S4a,c). On the other hand, we can notice that the J_{sc} increases just for treatment concentrations up to 20 mM (Figure S4b). Consequently, the optimal treatment conditions were reached for 20 mM when all the photovoltaic parameters simultaneously improved. In these conditions, the best performing small area PSCs achieved a PCE of 19.0%. The current density–voltage (J–V) curve of the champion untreated and treated-MAPbI₃ PSCs is reported in Figure 2b and the photovoltaic values are given in Table 4. Both the J_{sc} and the FF sensibly improved after the treatment: this trend is in agreement with our previously reported results [12].

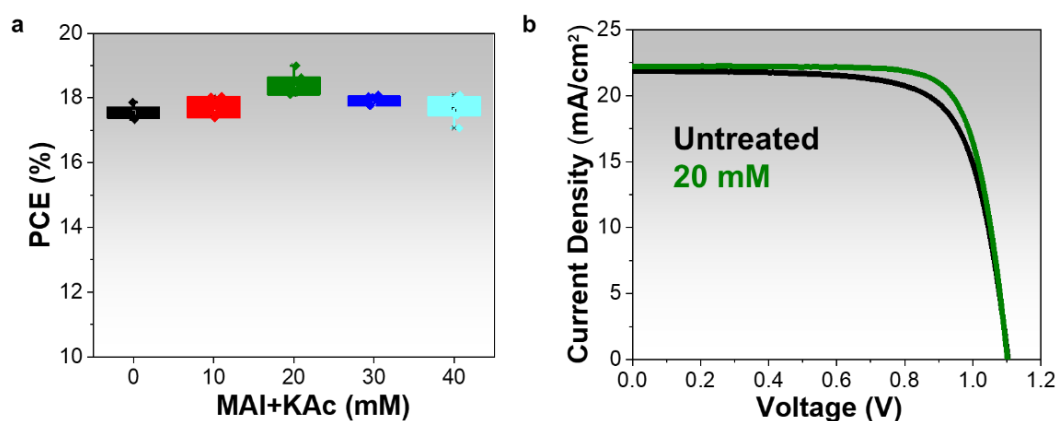


Figure 2. MAI + KAc treatment on MAPbI₃ n-i-p PSCs. (a) PCE statistics of the small area PSCs as a function of the MAI/KAc treatment concentration, and (b) current density–voltage (J–V) curves of the champion untreated and treated MAPbI₃ PSCs.

When the combined MAI + KAc treatment is applied to the thin MAPbI₃ films, the perovskite shows enlarged grain sizes (150–300 nm), less pinholes, and a uniform coverage Figure S5. This method significantly improves the perovskite morphology so that it can give the best device performance. In particular, the MAI + KAc treatment with 20 mM concentration gives the best film morphology; instead, higher concentrations of the treatment seem to be detrimental for the thin film.

Using the same device architecture employed in the small area device, Figure 1a, and the optimized treatment conditions, we also realized larger PSCs with an active area of 1 cm^2 . Front side and backside photographs show the full PSCs grown on a $2.5\text{ cm} \times 2\text{ cm}$ substrate in Figure 3a. The J–V curves of the champion PSCs with 1 cm^2 , corresponding to a PCE of 18.1%, are reported in Figure 3b and the photovoltaic values are given in Table 5. Increasing the active areas from 0.16 to 1 cm^2 , the J_{sc} slightly drops. This is related to the slightly increased probability to have recombination centers and defects over the larger area. At the same time, the V_{oc} slightly increases. Similar growth has already been observed by different authors and it is mostly due to masking effects on PSCs of different sizes. Indeed, the relative discrepancy between the mask area and the full device area on the PSCs agrees with what has been previously demonstrated [12,32–34].

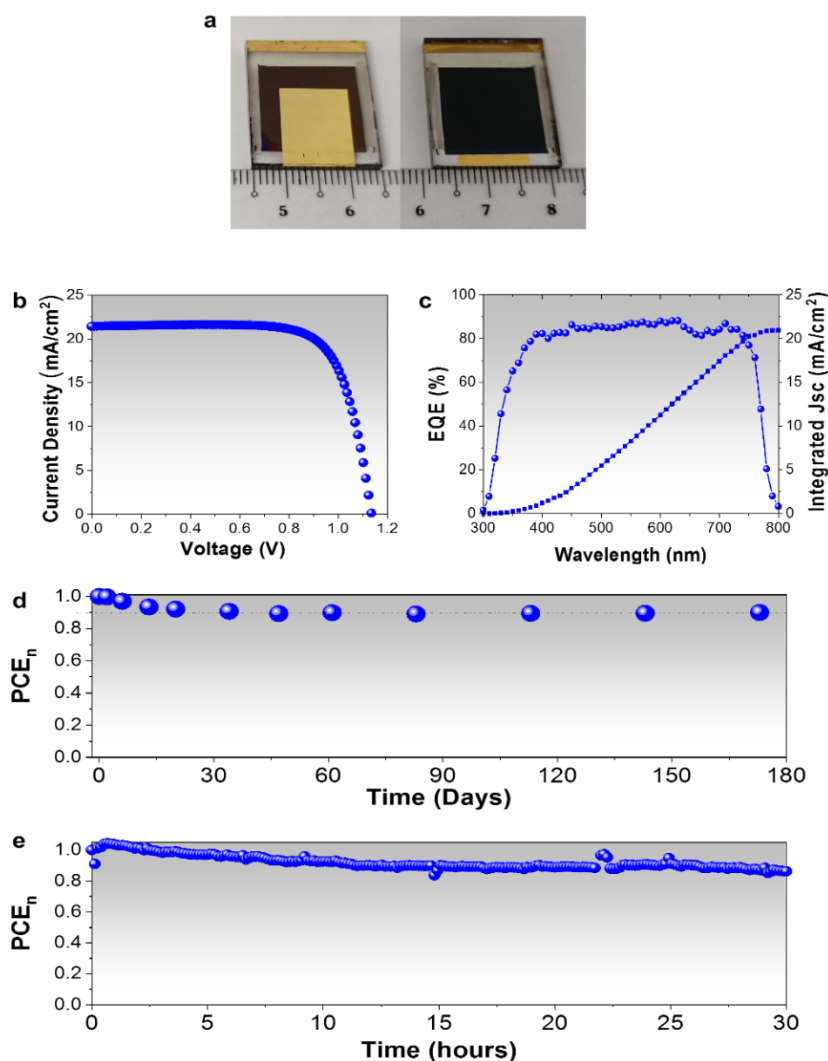


Figure 3. The 1 cm^2 treated-MAPbI₃ PSC. (a) Photograph of 1 cm^2 PSCs taken from both the front side and backside, (b) J–V curves under 1 sun illumination, (c) external quantum efficiency (EQE) spectra and its corresponding integrated current density over the whole spectra, (d) PSCs shelf stability when stored in ambient conditions with a controlled environment with 30% RH and (e) PSCs light stability under continuous light illumination at 1 sun (AM 1.5) without any temperature stabilization at an RH of 70%.

The slight PCE drop of 0.9% in absolute value, from 19.0% to 18.1%, is mainly due to the FF drop, from 77.4% to 74.7%, and is related to the increased sheet resistance of the transparent conductive oxides used to build the PSCs.

Table 4. PSCs' photovoltaic parameters of the MAPbI₃ PSCs with a combination of MAI + KAc treatment. The J_{sc}, V_{oc}, FF, and PCE average values were measured in backward scanning mode. PCEs for the champion PSCs are also reported.

MAI + KAc Treatment (mM)	V _{oc} ^{av} (V)	J _{sc} ^{av} (mA/cm ²)	FF ^{av} (%)	PCE ^{av} (%)	PCE ^{cham} (%)
0	1.099 ± 0.005	21.6 ± 0.3	72 ± 1.0	17.5 ± 0.4	17.9
10	1.10 ± 0.01	21.6 ± 0.4	74.1 ± 0.9	17.7 ± 0.3	18.0
20	1.105 ± 0.008	21.8 ± 0.4	76 ± 1.0	18.5 ± 0.5	19.0
30	1.106 ± 0.007	21.4 ± 0.3	76 ± 1.0	17.8 ± 0.3	18.1
40	1.108 ± 0.007	21.1 ± 0.5	75 ± 1.0	17.7 ± 0.5	18.1

Figure 3c shows that external quantum efficiency (EQE) spectra of the 1cm² PSCs is consistently above 80% for the whole spectra region where the PSCs absorb light. The integrated current density measured over the whole spectra (20.96 mA/cm²) agrees with the one measured from the J–V measurements and reported in Table 5.

The excellent long-term shelf stability of these un-encapsulated PSCs is reported in Figure 3d. Indeed, the PSCs maintain 90% of their initial PCEs for over six months when stored at ambient temperature (T = 25–28 °C) with a controlled RH of 30%. These results are impressive considering that these PSCs are un-encapsulated and contain MA. Moreover, Figure 3e shows that also under continuous light illumination at 1 sun (AM 1.5) the PSCs maintain over 80% of their initial PCE for over 30 h. It is worth to note that these measurements have been taken without any temperature stabilization and in the laboratory ambient with RH of 70%.

Table 5. PSCs' photovoltaic parameters of the treated-MAPbI₃ PSCs with different active areas. The J_{sc}, V_{oc}, FF, and PCE values were measured in backward scanning mode.

Active Area (cm ²)	J _{sc} (mA/cm ²)	V _{oc} (V)	FF (%)	PCE (%)
0.16	22.06	1.115	77.4	19.0
1	21.36	1.133	74.7	18.1

4. Conclusions

In this work, we have shown that the optimization process of the surface treatment based on both MAI and KAc on thermally evaporated MAPbI₃ thin films has driven high-performing thermally co-evaporated PSCs. This approach allowed us to demonstrate, n-i-p MAPbI₃ PSCs using TiO₂ as ETL with PCE of 19.0% and 18.1% for active areas of 0.16 cm² and of 1 cm², respectively. These are the highest reported values for thermally evaporated PSCs based on TiO₂ as ETL and Spiro-OMeTAD as HTL, for both small area and large area devices. Furthermore, these un-encapsulated PSCs also show a remarkable long-term shelf stability, maintaining 90% of their initial PCEs when stored at ambient temperature in a controlled environment with 30% RH.

These results confirm the high potential of the thermal evaporation technique for perovskite-based PSCs for realizing for large-area architecture with high PCEs with different architectures.

Supplementary Materials: The following are available online at <http://www.mdpi.com/2079-6412/10/12/1163/s1>, Figure S1: Photovoltaic parameters of the PSC with MAI treatment: (a) V_{oc}, (b) J_{sc}, and (c) FF, Figure S2: MAPbI₃ thin films morphology: FESEM top view of (a) as-deposited MAPbI₃ film, (b) MAPbI₃ film after MAI treatment, (c) MAPbI₃ film after KAc treatment, Figure S3: Photovoltaic parameters of the PSC without and with KAc treatment: (a) V_{oc}, (b) J_{sc}, and (c) FF, Figure S4: Photovoltaic parameters of the PSC with a combined MAI/KAc treatment: (a) V_{oc} (b) J_{sc} and (c) FF, Figure S5: MAPbI₃ thin films morphology: FESEM cross-section and top view of (a) as-deposited MAPbI₃ film; (b) MAPbI₃ film after MAI + KAc treatment, MAI + KAc concentration of 10 mM; (c) MAPbI₃ film after MAI + KAc treatment, MAI + KAc concentration of 20 mM; (d) MAPbI₃ film after MAI + KAc treatment, MAI + KAc concentration of 30 mM; (e) MAPbI₃ film after MAI + KAc treatment, MAI + KAc concentration of 40 mM.

Author Contributions: The work presented in this paper is a collaborative development by all of the authors. Conceptualization: J.L. and A.B.; methodology: J.L.; investigation: J.L., H.W., and H.A.D; resources: N.M., S.M., and A.B.; writing—original draft preparation: J.L. and A.B.; writing—review and editing: J.L, H.W., H.A.D., and A.B.; funding acquisition: N.M., S.M., and A.B. All authors have read and agreed to the published version of the manuscript.

Funding: This research is supported by the National Research Foundation, Prime Minister’s Office, Singapore under Energy Innovation Research Program (Grant numbers: NRF2015EWT-EIRP003-004, NRF-CRP14-2014-03, Solar CRP: S18-1176-SCRIP, NRF2018-ITC001-001).

Conflicts of Interest: Two of the authors N.M. and S.M. are directors of Prominence Photovoltaics Pte Ltd., a perovskite solar cell commercialization company. The other authors have no conflict of interests to declare.

References

1. Kim, D.; Jung, H.J.; Park, I.J.; Larson, B.W.; Dunfield, S.P.; Xiao, C.; Kim, J.; Tong, J.; Boonmongkolras, P.; Ji, S.G. Efficient, stable silicon tandem cells enabled by anion-engineered wide-bandgap perovskites. *Science* **2020**, *368*, 155–160. [CrossRef] [PubMed]
2. Chiang, Y.-H.; Anaya, M.; Stranks, S.D. Multisource Vacuum Deposition of Methylammonium-Free Perovskite Solar Cells. *ACS Energy Lett.* **2020**, *5*, 2498–2504. [CrossRef]
3. Zheng, X.; Hou, Y.; Bao, C.; Yin, J.; Yuan, F.; Huang, Z.; Song, K.; Liu, J.; Troughton, J.; Gasparini, N. Managing grains and interfaces via ligand anchoring enables 22.3%-efficiency inverted perovskite solar cells. *Nat. Energy* **2020**, *5*, 131–140. [CrossRef]
4. De Wolf, S.; Holovsky, J.; Moon, S.J.; Loper, P.; Niesen, B.; Ledinsky, M.; Haug, F.J.; Yum, J.H.; Ballif, C. Organometallic Halide Perovskites: Sharp Optical Absorption Edge and Its Relation to Photovoltaic Performance. *J. Phys. Chem. Lett.* **2014**, *5*, 1035–1039. [CrossRef] [PubMed]
5. Shi, D.; Adinolfi, V.; Comin, R.; Yuan, M.; Alarousu, E.; Buin, A.; Chen, Y.; Hoogland, S.; Rothenberger, A.; Katsiev, K.; et al. Low trap-state density and long carrier diffusion in organolead trihalide perovskite single crystals. *Science* **2015**, *347*, 519–522. [CrossRef]
6. Stranks, S.D.; Eperon, G.E.; Grancini, G.; Menelaou, C.; Alcocer, M.J.P.; Leijtens, T.; Herz, L.M.; Petrozza, A.; Snaith, H.J. Electron-Hole Diffusion Lengths Exceeding 1 Micrometer in an Organometal Trihalide Perovskite Absorber. *Science* **2013**, *342*, 341–344. [CrossRef] [PubMed]
7. Xing, G.; Mathews, N.; Sun, S.; Lim, S.; Lam, Y.; Grätzel, M.; Mhaisalkar, S.; Sum, T.; Grätzel, M. Long-Range Balanced Electron- and Hole-Transport Lengths in Organic-Inorganic $\text{CH}_3\text{NH}_3\text{PbI}_3$. *Science* **2013**, *342*, 344–347. [CrossRef] [PubMed]
8. Dong, Q.; Fang, Y.; Shao, Y.; Mulligan, P.; Qiu, J.; Cao, L.; Huang, J. Electron-hole diffusion lengths > 175 μm in solution-grown $\text{CH}_3\text{NH}_3\text{PbI}_3$ single crystals. *Science* **2015**, *347*, 967–970. [CrossRef]
9. Zheng, L.; Zhang, D.; Ma, Y.; Lu, Z.; Chen, Z.; Wang, S.; Xiao, L.; Gong, Q. Morphology control of the perovskite films for efficient solar cells. *Dalton Trans.* **2015**, *44*, 10582–10593. [CrossRef]
10. Zhao, Y.; Zhu, K. Organic–inorganic hybrid lead halide perovskites for optoelectronic and electronic applications. *Chem. Soc. Rev.* **2016**, *45*, 655–689. [CrossRef]
11. Dang, Y.; Ju, D.; Wang, L.; Tao, X. Recent progress in the synthesis of hybrid halide perovskite single crystals. *CrystEngComm* **2016**, *18*, 4476–4484. [CrossRef]
12. Li, J.; Wang, H.; Chin, X.Y.; Dewi, H.A.; Vergeer, K.; Goh, T.W.; Lim, J.W.M.; Lew, J.H.; Loh, K.P.; Soci, C.; et al. Highly Efficient Thermally Co-evaporated Perovskite Solar Cells and Mini-modules. *Joule* **2020**, *4*, 19. [CrossRef]
13. Liu, M.; Johnston, M.B.; Snaith, H.J. Efficient planar heterojunction perovskite solar cells by vapour deposition. *Nature* **2013**, *501*, 395–398. [CrossRef] [PubMed]
14. Momblona, C.; Gil-Escrig, L.; Bandiello, E.; Hutter, E.M.; Sessolo, M.; Lederer, K.; Blochwitz-Nimoth, J.; Bolink, H.J. Efficient vacuum deposited p-i-n and n-i-p perovskite solar cells employing doped charge transport layers. *Energy Environ. Sci.* **2016**, *9*, 3456–3463. [CrossRef]
15. Best Research-Cell Efficiency Chart. Available online: <https://www.nrel.gov/pv/cell-efficiency.html> (accessed on 28 November 2020).
16. Kojima, A.; Teshima, K.; Shirai, Y.; Miyasaka, T. Organometal Halide Perovskites as Visible-Light Sensitizers for Photovoltaic Cells. *J. Am. Chem. Soc.* **2009**, *131*, 6050–6051. [CrossRef]
17. Arora, N.; Dar, M.I.; Hinderhofer, A.; Pellet, N.; Schreiber, F.; Zakeeruddin, S.M.; Grätzel, M. Perovskite solar cells with CuSCN hole extraction layers yield stabilized efficiencies greater than 20%. *Science* **2017**, *358*, 768–771. [CrossRef]

18. Yang, S.; Chen, S.; Mosconi, E.; Fang, Y.; Xiao, X.; Wang, C.; Zhou, Y.; Yu, Z.; Zhao, J.; Gao, Y. Stabilizing halide perovskite surfaces for solar cell operation with wide-bandgap lead oxysalts. *Science* **2019**, *365*, 473–478. [[CrossRef](#)]
19. Wang, Y.; Wu, T.; Barbaud, J.; Kong, W.; Cui, D.; Chen, H.; Yang, X.; Han, L. Stabilizing heterostructures of soft perovskite semiconductors. *Science* **2019**, *365*, 687–691. [[CrossRef](#)]
20. Yang, W.S.; Noh, J.H.; Jeon, N.J.; Kim, Y.C.; Ryu, S.; Seo, J.; Seok, S.I. High-performance photovoltaic perovskite layers fabricated through intramolecular exchange. *Science* **2015**, *348*, 1234–1237. [[CrossRef](#)]
21. Bi, D.; Tress, W.; Dar, M.I.; Gao, P.; Luo, J.; Renevier, C.; Schenk, K.; Abate, A.; Giordano, F.; Correa Baena, J.-P.; et al. Efficient luminescent solar cells based on tailored mixed-cation perovskites. *Sci. Adv.* **2016**, *2*, e1501170. [[CrossRef](#)]
22. Saliba, M.; Matsui, T.; Seo, J.-Y.; Domanski, K.; Correa-Baena, J.-P.; Nazeeruddin, M.K.; Zakeeruddin, S.M.; Tress, W.; Abate, A.; Hagfeldt, A.; et al. Cesium-containing triple cation perovskite solar cells: Improved stability, reproducibility and high efficiency. *Energy Environ. Sci.* **2016**, *9*, 1989–1997. [[CrossRef](#)] [[PubMed](#)]
23. Saliba, M.; Matsui, T.; Domanski, K.; Seo, J.-Y.; Ummadisingu, A.; Zakeeruddin, S.M.; Correa-Baena, J.-P.; Tress, W.R.; Abate, A.; Hagfeldt, A.; et al. Incorporation of rubidium cations into perovskite solar cells improves photovoltaic performance. *Science* **2016**, *354*, 206–209. [[CrossRef](#)] [[PubMed](#)]
24. McMeekin, D.P.; Sadoughi, G.; Rehman, W.; Eperon, G.E.; Saliba, M.; Hörlantner, M.T.; Haghighirad, A.; Sakai, N.; Korte, L.; Rech, B.; et al. A mixed-cation lead mixed-halide perovskite absorber for tandem solar cells. *Science* **2016**, *351*, 151–155. [[CrossRef](#)] [[PubMed](#)]
25. Chen, H.; Ye, F.; Tang, W.; He, J.; Yin, M.; Wang, Y.; Xie, F.; Bi, E.; Yang, X.; Gratzel, M.; et al. A solvent- and vacuum-free route to large-area perovskite films for efficient solar modules. *Nature* **2017**, *550*, 92–95. [[CrossRef](#)] [[PubMed](#)]
26. Leyden, M.R.; Jiang, Y.; Qi, Y. Chemical vapor deposition grown formamidinium perovskite solar modules with high steady state power and thermal stability. *J. Mater. Chem. A* **2016**, *4*, 13125–13132. [[CrossRef](#)]
27. Jiang, Y.; Leyden, M.R.; Qiu, L.; Wang, S.; Ono, L.K.; Wu, Z.; Juarez-Perez, E.J.; Qi, Y. Combination of Hybrid CVD and Cation Exchange for Upscaling Cs-Substituted Mixed Cation Perovskite Solar Cells with High Efficiency and Stability. *Adv. Funct. Mater.* **2018**, *28*. [[CrossRef](#)]
28. Chen, B.; Zhengshan, J.Y.; Manzoor, S.; Wang, S.; Weigand, W.; Yu, Z.; Yang, G.; Ni, Z.; Dai, X.; Holman, Z.C. Blade-coated perovskites on textured silicon for 26%-efficient monolithic perovskite/silicon tandem solar cells. *Joule* **2020**, *4*, 850–864. [[CrossRef](#)]
29. Forgács, D.; Gil-Escrig, L.; Pérez-Del-Rey, D.; Momblona, C.; Werner, J.; Niesen, B.; Ballif, C.; Sessolo, M.; Bolink, H.J. Efficient Monolithic Perovskite/Perovskite Tandem Solar Cells. *Adv. Energy Mater.* **2017**, *7*, 1602121. [[CrossRef](#)]
30. Sahli, F.; Werner, J.; Kamino, B.A.; Brauning, M.; Monnard, R.; Paviet-Salomon, B.; Barraud, L.; Ding, L.; Diaz Leon, J.J.; Sacchetto, D.; et al. Fully textured monolithic perovskite/silicon tandem solar cells with 25.2% power conversion efficiency. *Nat. Mater.* **2018**, *17*, 820–826. [[CrossRef](#)]
31. Abdi-Jalebi, M.; Andaji-Garmaroudi, Z.; Cacovich, S.; Stavarakas, C.; Philippe, B.; Richter, J.M.; Alsari, M.; Booker, E.P.; Hutter, E.M.; Pearson, A.J.; et al. Maximizing and stabilizing luminescence from halide perovskites with potassium passivation. *Nature* **2018**, *555*, 497. [[CrossRef](#)]
32. Kiermasch, D.; Gil-Escrig, L.; Bolink, H.J.; Tvingstedt, K. Effects of masking on open-circuit voltage and fill factor in solar cells. *Joule* **2019**, *3*, 16–26. [[CrossRef](#)]
33. Dewi, H.A.; Wang, H.; Li, J.; Thway, M.; Lin, F.; Aberle, A.G.; Mathews, N.; Mhaisalkar, S.; Bruno, A. Four-Terminal Perovskite on Silicon Tandem Solar Cells Optimal Measurements Schemes. *Energy Technol.* **2020**, *11*, 34178–34187. [[CrossRef](#)]
34. Li, J.; Dewi, H.A.; Wang, H.; Lew, J.H.; Mathews, N.; Mhaisalkar, S.; Bruno, A. Design of Perovskite Thermally Co-Evaporated Highly Efficient Mini-Modules with High Geometrical Fill Factors. *Sol. Rrl* **2020**, 2000473. [[CrossRef](#)]

Publisher’s Note: MDPI stays neutral with regard to jurisdictional claims in published maps and institutional affiliations.



© 2020 by the authors. Licensee MDPI, Basel, Switzerland. This article is an open access article distributed under the terms and conditions of the Creative Commons Attribution (CC BY) license (<http://creativecommons.org/licenses/by/4.0/>).